Active nematic order and dynamic lane formation of microtubules driven by membrane-bound diffusing motors

Fereshteh L. Memarian[a], Joseph D. Lopes[a], Fabian Jan Schwarzendahl[a,b], Madhuvanthi Guruprasad Athani[a], Niranjan Sarpangala[a], Ajay Gopinathan[a], Daniel A. Beller[a], Kinjal Dasbiswas[a], and Linda S. Hirst[a,1]

[a]Department of Physics, University of California, Merced, CA 95343; and [b]Institut für Theoretische Physik II: Weiche Materie, Heinrich-Heine-Universität Düsseldorf, D-40225 Düsseldorf, Germany

Edited by Andreas Bausch, Lehrstuhl für Zellbiophysik E27, Technical University Munich, Garching, Germany; received September 23, 2021; accepted October 21, 2021 by Editorial Board Member Mehran Kardar

Dynamic lane formation and long-range active nematic alignment are reported using a geometry in which kinesin motors are directly coupled to a lipid bilayer, allowing for in-plane motor diffusion during microtubule gliding. We use fluorescence microscopy to image protein distributions in and below the dense two-dimensional microtubule layer, revealing evidence of diffusion-enabled kinesin restructuring within the fluid membrane substrate as microtubules collectively glide above. We find that the lipid membrane acts to promote filament–filament alignment within the gliding layer, enhancing the formation of a globally aligned active nematic state. We also report the emergence of an intermediate, locally ordered state in which apolar dynamic lanes of nematically aligned microtubules migrate across the substrate. To understand this emergent behavior, we implement a continuum model obtained from coarse graining a collection of self-propelled rods, with propulsion set by the local motor kinetics. Tuning the microtubule and kinesin concentrations as well as active propulsion in these simulations reveals that increasing motor activity promotes dynamic nematic lane formation. Simulations and experiments show that, following fluid bilayer substrate mediated spatial motor restructuring, the total motor concentration becomes enriched below the microtubule lanes that they drive, with the feedback leading to more dynamic lanes. Our results have implications for membrane-coupled active nematics in vivo as well as for engineering dynamic and reconfigurable materials where the structural elements and power sources can dynamically colocalize, enabling efficient mechanical work.

active matter | liquid crystal | active nematic | biopolymers

Materials formed from biopolymers and molecular motors represent a distinct type of active matter assembled from molecular components extracted from biological cells. Similar to other recently developed active systems such as self-driven colloids, or the ubiquitous examples from nature (bees swarming, birds flocking, bacterial colonies), biologically derived active systems must incorporate an energy-transducing element to drive their collective motion. All these different active systems are intrinsically out of equilibrium, forming dynamic steady states that fluctuate and evolve in a manner quite distinct from the familiar equilibrium materials described by classical thermodynamics (1–3). In particular, the motility of individual agents alone can induce phase separation without requiring specific attractive interactions. Biopolymer-based active systems combine the shape anisotropy and active propulsion of individual agents. This can lead to more complex collective spatiotemporal pattern formations which have been explored with active matter theories (4–6). Two biopolymer-based active systems in particular have recently drawn the attention of researchers for exhibiting a wide range of novel fundamental phenomena: actin filaments with myosin motors (7–10) and microtubules with kinesin motors (1, 10–14).

In the eukaryotic cell, microtubules and molecular motors are central to intracellular transport and cell division. Microtubules (MTs) are protein filaments that assemble from tubulin dimers into a 25-nm-diameter hollow tube up to >10 μm in length with a defined polarity (distinct negative and positive ends). (1). Nanoscale motor proteins, such as kinesin and dynein, convert the cell's chemical energy source, adenosine triphosphate (ATP), into mechanical energy and effectively "walk" along the MT in a processive motion from one end of the MT to the other (1, 15, 16). Kinesin motor proteins are ∼60 nm in size and take 8-nm steps in a stochastic, processive motion to transport cargos (i.e., lipid vesicles or organelles) by acting individually or in groups (17–19). These out-of-equilibrium cellular mechanisms have provided inspiration for a variety of novel in vitro experiments in recent years and biopolymers with molecular motors have been used to create some of the first examples of molecular-scale active phases. In a particularly significant example from the recent literature, two-dimensional active nematic assemblies arise from locally aligned MTs self-assembled into polar bundles, which bind to kinesin motor clusters and slide relative to each other. (20) The result is a dynamic MT fluid that exhibits mobile topological

Significance

Active nematics are ordered liquid crystalline fluids that exhibit spontaneous persistent flows and collective dynamics. The development of motile biopolymer systems inspired by nature has recently attracted considerable attention to out-of-equilibrium soft materials. We report the formation of an active nematic in which microtubules are propelled by kinesin motors coupled to a lipid membrane substrate. The system exhibits apolar order in a globally aligned nematic phase and locally ordered dynamic lanes. Use of a fluid substrate represents a significant advance for active matter as it allows for spatial re-organization of motors, which generate force, in response to the dynamics of the aligning microtubules. This self-organized feedback mechanism may have implications in vivo and for engineering efficient dynamic and reconfigurable materials.

Author contributions: A.G., D.A.B., K.D., and L.S.H. designed research; F.L.M., J.D.L., F.J.S., M.G.A., and N.S. performed research; F.L.M., F.J.S., M.G.A., and N.S. analyzed data; and F.L.M., F.J.S., D.A.B., K.D., and L.S.H. wrote the paper.

The authors declare no competing interest.

This article is a PNAS Direct Submission. A.B. is a guest editor invited by the Editorial Board.

This open access article is distributed under Creative Commons Attribution-NonCommercial-NoDerivatives License 4.0 (CC BY-NC-ND).

[1]To whom correspondence may be addressed. Email: lhirst@ucmerced.edu.

This article contains supporting information online at http://www.pnas.org/lookup/suppl/doi:10.1073/pnas.2117107118/-/DCSupplemental.

Published December 21, 2021.

defects and self-driven chaotic mixing (21) characterized by the braiding of topological defects in two dimensions and complex defect loop dynamics in three dimensions (22).

Other geometric configurations of biopolymers and motors can be adopted to produce a variety of new active states of self-propelled units, analogous to the phenomena seen in flocks and swarms (13). The classic gliding assay experiment, traditionally used to quantify molecular motor activity, has been recently adopted by soft-matter scientists to study the collective motion of motor-driven filaments. In this configuration, the motors are bound to a surface and couple to MTs that are propelled by the motor-stepping action below. Interactions between the MTs and motors lead to a variety of interesting phenomena. Self-binding MTs can curl around on each other to form "spools" or rotating loops that continually turn as long as ATP is present (11). At high enough concentrations, global nematic order can emerge in the MT or actin layer, purely due to lateral steric interactions and activity, creating an active nematic system of self-propelled filaments (23–25). These experimental results have recently been explored theoretically with agent-based simulations producing polar and apolar nematics and motile polar clusters (26–29).

In this paper our experiments and simulations are based on a variant of the standard gliding assay; the motor proteins are not immobilized on the substrate but are instead embedded in a fluid lipid bilayer. Fig. 1*A* illustrates the experimental geometry. When biopolymers are introduced to the flow cell, the motors bind to the MT filaments and, in the presence of ATP, exert directional forces to transport them across the motor-decorated surface. Bilayer coupling has been previously used to study single MT dynamics (17, 18) and in a recent paper (30) membrane coupling was used to generate active alignment in an F-actin filament layer, producing fascinating polar liquid crystalline patterns. In this work we report the formation of dense apolar MT nematics and lanes on a lipid bilayer with accompanying theoretical modeling. The bilayer enhances filament active bundling, consistent with ref. 24, and notably for our work the lipid bilayer also allows the motors to disperse via lateral diffusion as they bind, walk on, and release from the MTs they encounter in an ATP-dependent fashion (18).

Use of this fluid substrate adds a new level of complexity to the collective gliding motion. MT gliding velocities depend on local motor concentration, generating a feedback between motor concentration and MT density. The gliding process acts to redistribute motors in the membrane in a way that would be impossible for fixed motors on a nondiffusive substrate.

Lipid Bilayer-Coupled Gliding Assays

Fig. 1*A* illustrates the experimental configuration. Motor proteins are coupled to lipids in the upper leaflet of a supported lipid bilayer via a *His* tag. We selected a simple DOPC lipid bilayer with fluid-like properties at room temperature for the substrate and incorporated 10 mol % DGS-NTA lipids (Avanti Polar lipids) as binding sites for *His*-tagged kinesin. The flow cell can be filled with different solutions and aqueous buffers (see *Materials and Methods*), allowing for the sequential introduction of proteins and wash solutions after bilayer deposition. We confirmed, using fluorescence recovery after photobleaching (FRAP), that the membrane-bound motors were able to

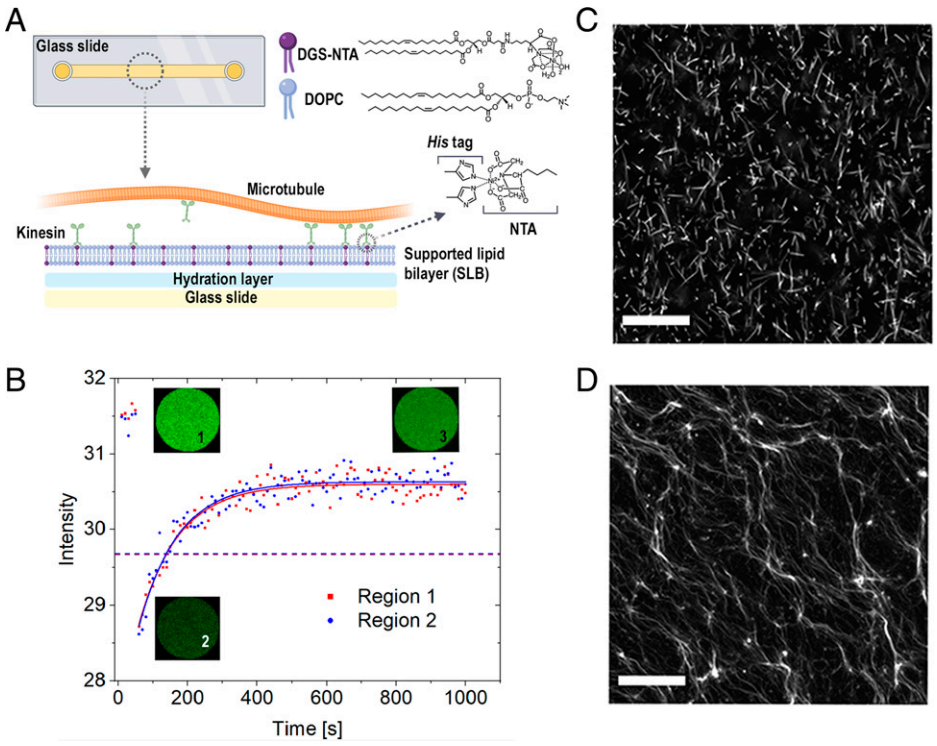

Fig. 1. Experimental geometry for gliding assay on a lipid bilayer and comparison with a glass substrate. (*A*) Schematic view of the experimental geometry. A supported lipid bilayer is deposited in a fully hydrated flow cell. Motor proteins bind to the DGS-NTA(Ni) lipids in the membrane, propelling the MTs across the membrane surface. (*B*) Due to the fluidity of the membrane the motor proteins may diffuse laterally in the bilayer. FRAP is used to measure kinesin lateral diffusion in the lipid bilayer [10 mol % DGS-NTA(Ni) and 90 mol % DOPC]. D_{KIN} = 1.72 ± 0.27 μm^2/s. FRAP images at the bleach spot on the lipid bilayer indicate (1) fluorescence intensity before photobleaching, (2) immediately after bleaching, and (3) after recovery. (For details see *Materials and Methods*.) (*C* and *D*) Fluorescence images of MTs (average length, 7.30 μm ± 0.73) gliding on glass vs. the supported lipid bilayer. MT concentration in both experiments is 0.27 mg/mL (6.9% of the filaments fluorescently labeled) with a kinesin concentration of 300 nM. Each panel is an overlay of 10 consecutive frames (total time = 50 s). (*C*) MTs gliding on glass without depletant; the MT distribution is isotropic and exhibits widespread crossing behavior. (*D*) Gliding on a lipid bilayer, MTs display increased active bundling, orientational order, and collective motion. (Scale bars, 50 μm.)

diffuse with a diffusion constant, D_{KIN}, of 1.72 ± 0.27 $\mu m^2/s$, a number comparable to others reported using similar measurements (Fig. 1*B* and *Materials and Methods*) (12, 15).

Active Bundling Is Promoted by the Lipid Bilayer, Inducing Nematic Ordering and Lane Formation

A challenge in designing active phases in this two-dimensional (2D) geometry comes from the propensity of MTs to glide over each other when they collide, instead of aligning with each other (21). Order, whether polar or nematic, is promoted if the MTs remain primarily in the 2D plane. If the advancing MT encounters another MT, two collision types are possible (Fig. 2*A*): a "crossing" event (where one MT glides over the top of the other, exhibiting minimal deviation from its original trajectory) or "active bundling" (21), where the two incident MTs spontaneously align with each other, subsequently moving parallel or antiparallel to each other. To promote orientational order in gliding MTs, as opposed to an active isotropic state, crossing events should be reduced. To diminish the frequency of crossings, a depletion agent, such as polyethylene glycol (PEG), in the solution above the gliding layer has been used in other works (21, 22, 25). Here, we show that the use of a lipid bilayer alone as the substrate can produce a similar effect, without the need for a depletant.

Fig. 1 *C* and *D* qualitatively contrast MT gliding on glass and on a lipid bilayer at the same MT and kinesin concentrations at steady state. On glass, no local or global alignment is present, but changing the substrate to a fluid lipid bilayer produces nematic order. To connect the effect of the bilayer on MT interactions and phase ordering we performed a statistical analysis on collision events between pairs of MTs (Fig. 2 *B* and *C*) comparing gliding on a glass substrate with gliding on the lipid bilayer, in both cases without depletant. The experiment revealed a clear difference in collision statistics between the two substrates. Gliding on a glass substrate produced active bundling events predominantly at low angles of approach (close to 0° or 180°), with crossing events being much more likely and favored at high approach angles (close to 90°). In contrast, the lipid bilayer produced a much higher probability of active bundling overall, and collisions at high angles were much more likely to result in active bundling events. These results support the conclusion that active bundling is promoted by the lipid bilayer and therefore that the bilayer supports formation of an active nematic phase. We note, however, that crossings are not completely suppressed by the presence of the bilayer and that further suppression of crossings may lead to additional collective phases, such as the polar phases observed or predicted in previous works (24, 25, 29–31).

Emergence of Global Nematic Order and Locally Ordered Lanes

We investigated the steady-state collective behavior of the membrane-bound MTs over a range of MT and ATP concentrations using fluorescence microscopy. All movies analyzed were recorded using a population in which only 1.8 to 13% of the total MTs were fluorescently labeled (i.e., 98.2 to 93.1% of the MTs are not visible under fluorescence microscopy). The labeling method was chosen such that the director field could be easily visualized. Labeled MTs act as tracers to visualize the overall active flows.

We observed four different steady states, as presented in the qualitative phase diagram in Fig. 3*A* along with representative images (Fig. 3*B*): isotropic, locally ordered lanes, a globally ordered nematic state, and a coexistence state of lanes and the nematic phase. We observed that MT surface concentration was a strong factor in determining the existence of nematic ordering and that increasing the MT average velocity had a weaker effect and tended to decrease the order. Velocity was varied using ATP concentration in a manner consistent with Michalis–Menten kinetics (32) (see *SI Appendix*, Fig. S8). At higher MT concentrations we observed global nematic ordering of the filaments. At low MT concentrations, a generally disordered isotropic state was characteristic. Most interestingly, we observed that the dynamic lanes of locally aligned MTs arise as an intermediate state (Movies S1–S3) within a particular MT concentration range that depends on the ATP concentration (Fig. 3 *A*, orange shading). On the global scale, the overall MT orientation distribution is isotropic in this state, with lanes dynamically migrating across the substrate. In the coexistence state, the lanes become oriented in a global direction while the density remains inhomogeneous. In all

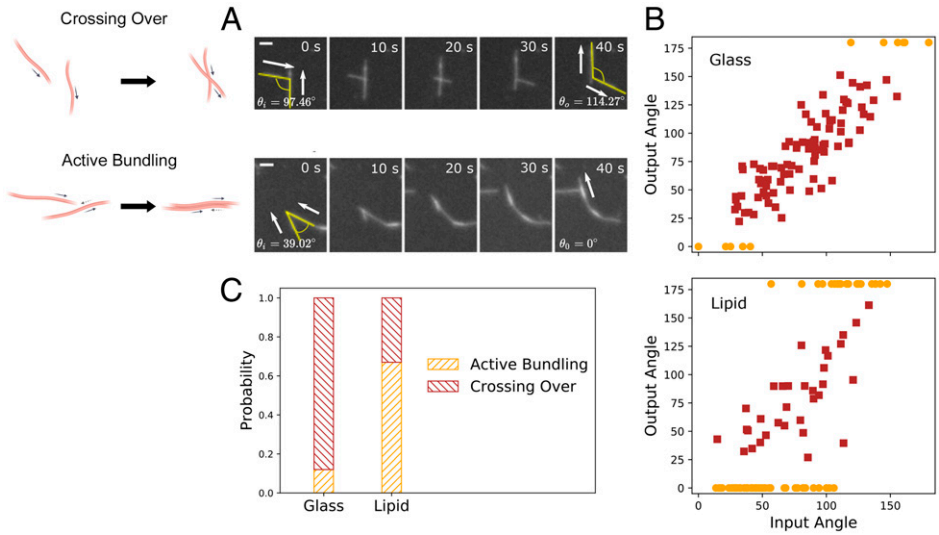

Fig. 2. MT collision statistics comparing glass and lipid substrates. (*A*) Snapshots from fluorescence microscope movies showing the two types of collision events: crossing over and active bundling. Input angle q_i between filaments before collision, and output angle q_o after collision are as shown. (Scale bars, 10 μm.) (*B*) Input and output angles (in degrees) for 100 collision events each on glass and lipid substrates, classified based on their collision type, crossing over (red squares), and active bundling (orange circles). (*C*) The probability of collisions resulting in active bundling or crossing over on glass and lipid substrates computed from the data in *B*.

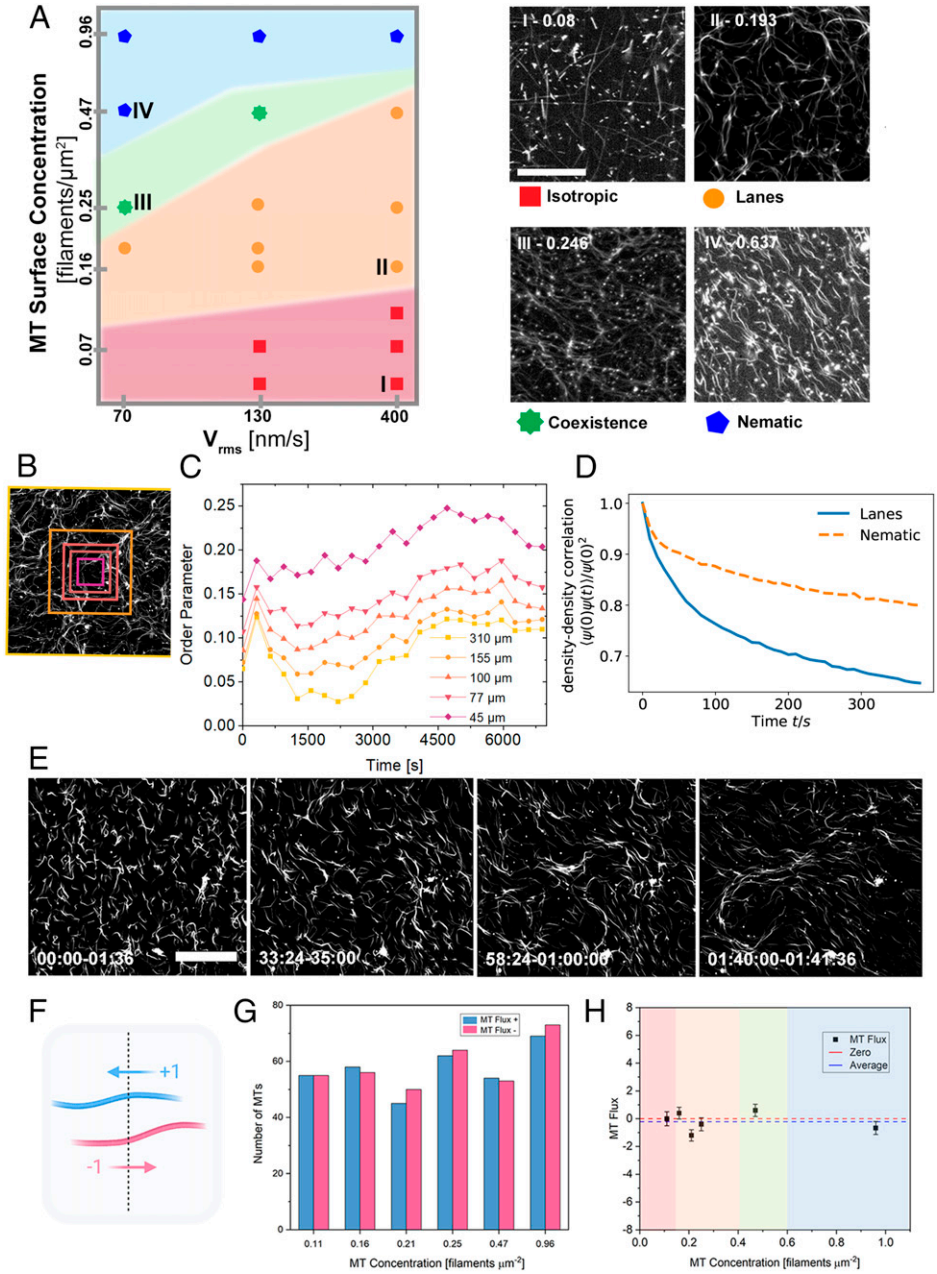

Fig. 3. Emergence of global nematic order and locally ordered lanes. (*A*) Phase diagram demonstrating the effects of MT organization and ATP concentration on the collective motion of membrane-bound MTs where 1.8 to 13% of MTs are fluorescently labeled and visible in the images (concentration of labeled MTs 0.0125 mg/mL). (Scale bar, 50 μm.) Images to the right are representative fluorescence micrographs for the steady state behavior of the system under different conditions as labeled on the phase diagram (I = 0.5 mM ATP, 0.05 mg/mL MT, II = 0.5 mM ATP, 0.16 mg/mL MT, III = 0.05 mM ATP, 0.27 mg/mL MT, and IV = 0.05 mM ATP, 0.40 mg/mL MT. Each image panel shows a combined stack of 100 frames recorded 60 min after the start of the experiment; this visualization highlights the collective motion. At higher MT densities, a steady-state global nematic alignment predominates, whereas somewhat lower MT concentrations produce apolar lane formation. Increasing ATP increases gliding velocity, but it does not have a strong effect on phase morphology. (*B* and *C*) Nematic order parameter calculation as a function of length scale for five different ROI sizes (0.096 mm^2, 0.024 mm^2, 0.01 mm^2, 0.006 mm^2, and 0.002 mm^2) as shown in *B*. The initial drop for all box sizes likely corresponds to the decay of flow induced alignment immediately after flow cell filling (0 to 15 min). Later we see that the texture becomes more ordered on local length scales, compared to the global measure (yellow box); this indicates the time-dependent formation of lanes. (Scale bar, 50 μm.) (*D*) Density–density correlation function calculated for the experimental steady-state global nematic (a IV) and lane state (a II) as a function of time. ψ is the density of filaments. (*E*) Time sequence of fluorescence microscope images demonstrating the disorder–order transition from an isotropic state to locally aligned lanes over a total period of 48 min and 30 s (6.9% of the filaments fluorescently labeled). Each image is a combined time-stack of 10 consecutive image frames. After 30 min local alignment and dynamic apolar lanes begin to form and gradually become more ordered. MT concentration = 0.18 mg/mL and kinesin concentration = 300 nM. (Scale bar, 50 μm.) (*F–H*) Apolar motion of MTs. (*F*) Schematic showing gliding MT flux measurements across a plane indicated by the dashed line. (*G*) Bar chart plotting the total number of MTs crossing in either the positive or negative direction (+1 or −1). For each MT concentration, five regions on the microscope slide were selected. In each region the MTs were counted crossing the plane over five different 10-s time intervals and combined. (*H*) Total flux as a function of MT concentration calculated from data in *G*. The graph indicates phase using colors corresponding to the phase diagram in *A*.

phases the order is apolar, with MTs gliding in both the positive and negative directions parallel to the local nematic director (Fig. 3 and Movie S2).

In our experiments, active filament ordering emerges over time from an initially isotropic state in a dense layer of gliding MTs, as shown by the time sequence in Fig. 3*F*. In this figure the nematic order is not global but instead appears in the form of locally ordered lanes along which MTs move bidirectionally. To highlight the alignment of the filaments each image in the sequence is prepared as a time stack of 10 consecutive movie frames. The images, taken from Movie S1, demonstrate the transition from an isotropic state at $t = 0$ (where filaments show no orientational ordering) to a state with significant local orientational order 30 min after introducing MTs to the flow cell.

To show the onset of the laning state in more detail, we calculated a time-dependent nematic order parameter over five different length scales indicated by the colored boxes overlaying the example image in Fig. 3*C* (see *Materials and Methods*). Lanes are locally aligned, but their orientations are isotropic over larger length scales. At steady state we found that a larger box size produced a lower-order parameter, in good agreement with our visual assessment of the videos; lanes exhibit local apolar order (MTs are aligned, gliding both up and down the lane), but due to the dynamic isotropic arrangement of the lanes, there is low global orientational order. The graph also highlights the time dependence of the order parameter over different length scales. The videos were recorded shortly after the introduction of MTs to the flow cell. For all length scales analyzed, the order parameter is initially high then reduces and subsequently increases again. We can interpret this behavior as a consequence of initial flow alignment in the flow cell. Over time the system loses this initial order, then on formation of the active laning state the order parameter becomes more length-scale-dependent. We thus find an unexpected time sequence of active states in which global nematic order with uniform density is unstable to isotropic disorder, which in turn is unstable to the formation of lanes with local nematic order. Fig. 3*E* shows a calculation of the density–density correlation function $<\psi(0)\ \psi(t)>$ for these experimental results comparing the global nematic state and the lane state. This comparison demonstrates that the lanes are more dynamic than the global nematic state, in which lane structures form and dissolve on a time scale of 100s of seconds (Movie S1).

We can understand the formation of locally ordered lanes as a consequence of the active motor-induced motility of the filaments together with the active bundling phenomenon. A filament encountering a higher-density "lane" region with alignment will actively bundle with filaments already in the lane and thus reorient along the lane's director. Frequent subsequent collisions with other filaments in the lane reinforce this alignment, suppressing the effective rotational diffusion experienced by an isolated active filament. Filaments within lanes are less likely to escape due to their high aspect ratio and low rotational diffusion. Thus, filaments can easily glide into the lanes but cannot glide out as easily and are effectively trapped. The local order within lanes occurs analogously with thermally equilibrated systems of sterically repelling rods whose order is described by Onsager's theory (33) for a density-controlled isotropic–nematic phase transition, but here the order is caused by the active collisions of filaments. In the gliding filament assay, the density variations are reinforced by activity which drives positive feedback between filament density and oriented motion.

The locally ordered lanes in our system are similar in structure to lanes or bands observed previously in filament-motor gliding systems with depletants and in agent-based simulations (24, 34). However, here the lanes are not stable, but dynamic, as they are seen to move around the substrate, dissolve, and reform. Further, the density of motors and therefore the active propulsion of the rods can be spatially inhomogeneous because of the diffusivity of motors on the novel membrane substrate. To better understand these lane dynamics, we next compared our experiments to a continuum theoretical model that includes motor dynamics.

Continuum Model Simulations of Rods Driven by Motors Show Active Apolar Lanes

To better understand the mechanisms behind the origin and dynamics of the nematic lanes, we designed a computational, continuum model based on a coarse graining of a minimal model in which the MTs are represented by rods, driven by point-like (kinesin) motors (35) and incorporating the binding–unbinding and diffusive dynamics of motors. See *Materials and Methods* and *SI Appendix* for mathematical details. This computational model sheds light on the peculiar sequence of active states observed experimentally. Consistent with the experiments, our computational results suggest that with increasing motor activity (i.e., self-propulsion velocity v of the rod-like filaments) the uniform nematic system is susceptible to a breakup into nematic lanes (Fig. 4).

We write the governing equations, given in *Materials and Methods*, in terms of three fields describing the configuration of the MTs: the density ψ, the polar order $\boldsymbol{p}$, and the nematic order tensor $\boldsymbol{Q}$. These are based on coarse-graining microscopic equations of motion for self-propelled rods and embody the basic principles of conservation and symmetry. The density and nematic order are advected in the direction set by the polarization, which in turn is oriented by gradients of density and nematic order. Higher density in the model induces nematic order through a phenomenological Landau–de Gennes free energy that complements the active terms. Taken together, these give rise to the instability to lane formation. The propulsion velocity is also taken to be proportional to the local concentration of motors bound to filaments and is thus a spatially nonuniform fraction of a saturation speed v_0 set by individual motor activity, as described later.

By considering the continuum model for a collection of rods that are uniformly self-propelled at the saturation speed, v_0, we perform a linear stability analysis of the density and nematic order about the uniform nematic state, $\psi = \psi_0 + \delta\psi$, and $\boldsymbol{Q} = \boldsymbol{Q}_0 + \boldsymbol{\delta Q}$, where ψ_0 induces global nematic order $Q_{0,ij} = S_0\left(n_{0,i}n_{0,j} - \frac{1}{2}\delta_{ij}\right)$, aligned along a fixed unit vector, $\boldsymbol{n}_0$. The fastest-growing modes of the perturbed fields, $\delta\psi$ and $\boldsymbol{\delta Q}$, are captured by the real part of the largest eigenvalue (max [Re(ω)]) of the system of linearized dynamic equations (see *SI Appendix* for details), which is plotted in Fig. 4*A* for varying propulsion speed v_0. Our calculation of max [Re(ω)] shows that it becomes positive at a critical value of v_0, indicating the onset of the laning instability. Indeed, as we increase v_0 in our simulations beyond the value predicted by our stability analysis, lanes appear in the system, as shown in Fig. 4*A*, *Insets*. At even higher activity, the lanes become dynamic, since motility-induced patterns are expected to be transient, and chaotic instabilities are also a generic feature of active nematic systems (15). Such transitions into lanes and chaotic dynamics of the lanes have also been reported in agent-based simulations of polar rods with nematic alignment (34, 36–38) and predicted by hydrodynamic models (39–41).

To see how MT and ATP concentration affect the collective behavior of MTs, we numerically simulated our continuum model at different values of filament density and propulsion speed (see *SI Appendix* for table of parameter values). Fig. 4*B* shows the collective phases for varying average filament density ψ_c and the characteristic self-propulsion velocity. Representative simulation snapshots are shown in Fig. 4 *C*–*F* for each of

PHYSICS

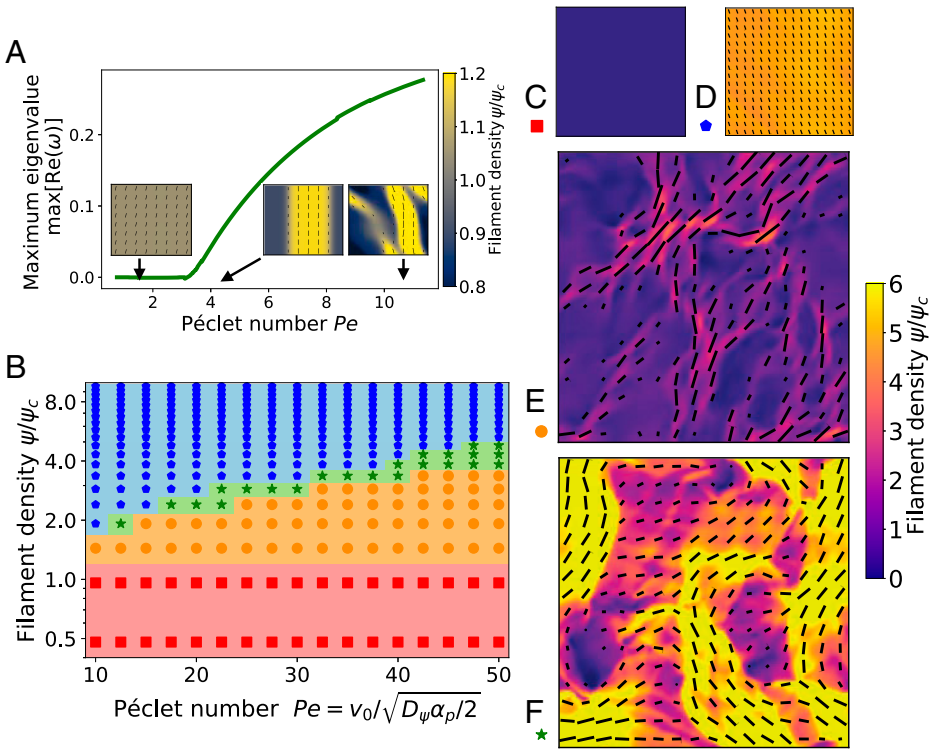

Fig. 4. Continuum model predictions and simulation results for active nematic lane formation. (*A*) Onset of laning. Linear stability analysis of the continuum model about a uniform nematic state showing the maximum real part of the eigenvalue [Re(ω)] which corresponds to the fastest-growing mode. A positive value beyond a critical propulsion speed (motor activity) indicates instability to lane formation. (*Insets*) Simulation snapshots below (*Left*), above (*Middle*), and far above (*Right*) the theoretically predicted onset of lane formation. Here, the color shows local filament density, and the black lines show the local nematic director field. (*B*) Nonequilibrium phase diagram for collective dynamics obtained from numeric simulations of the continuum model at different values of average filament density (MT concentration) and Péclet number representing the ratio of filament propulsion to diffusion in the system. The simulation results are classified according to overall nematic order using the same criteria as experiments. Representative snapshots with color code corresponding to local density are shown for each case: (*C*) isotropic, (*D*) nematic, (*E*) lanes, and (*F*) coexistence. Like in the experiments, higher filament density induces the nematic phase, while higher propulsion speeds corresponding to increased motor activity (higher ATP concentration) favor the breakup of the global nematic into lanes.

the four phases classified according to overall nematic order. In these, the color represents the local filament density $\psi(t)$. The density values are normalized by ψ_c, the critical density for the isotropic-to-nematic transition which we estimate to be ~ 0.1 filaments μm^{-2} from the Onsager theory of hard rods in thermal equilibrium (see *SI Appendix*) and which can be tuned in experiment by varying the average length of MTs. We note that ψ_c is a phenomenological parameter in the model that can in principle be very different from the Onsager threshold as observed in other gliding assay experiments (30), since the active bundling of filaments promotes their alignment whereas cross-overs can reduce this. We find that regions in which the filament density is enhanced form lane structures, which are locally nematic (nematic director field is shown as black lines). The results in Fig. 4 can be compared with the experimental images and phase diagram in Fig. 3. Consistent with the experiments, these simulations reveal that global nematic alignment occurs at sufficiently high MT concentrations and that increasing activity decreases the large-scale nematic order by promoting lanes that are locally ordered but isotropic in orientational distribution (24).

Diffusion Promotes Lane Dynamics and MT-Directed Motor Redistribution

One of the most striking features in this active system is the emergence of the steady state in which MTs form apolar ordered lanes or trails (Movies S1–S3). These lanes are dynamic and migrate across the substrate over time. Qualitatively similar behavior was also seen in actin/myosin-based active matter (24) and recently using MTs by Tsitkov et al. (42), but here motor diffusion has been examined as a possible control mechanism for active phases. To understand this potential mechanism we investigated correlations in spatial distributions of motors and filaments, in both experiments and simulations.

Motor proteins constantly bind and unbind from MTs during gliding. At the same time, these motors can diffuse in the lipid bilayer. They can bind and propel MTs then after a few steps fall off while remaining anchored to the fluid lipid layer. Fig. 5 *A–C* demonstrate how the gliding action of MTs can redistribute the lipid-bound motors during laning. In Fig. 5*A*, we observe a uniform distribution of labeled kinesin motors coupled to the bilayer (unlabeled MTs are present but not visible in these images). After 16 min, 30 s a clear difference is seen—the motor distribution is inhomogeneous and enriched in the area inside the green box. This motor restructuring on the substrate is made possible by in-plane diffusion. Thus, we find that the lipid-coupled motors are redistributed as a direct result of the gliding MTs (also see *SI Appendix*, Figs. S6 and S7).

This phenomenon is of particular interest, because the effect of motor diffusion on lane formation and dynamics has not previously been studied within the hydrodynamic theory. To model this, we assume that motors bind and unbind to filaments with some characteristic rates. When bound to filaments, motors propel the filaments actively with a propulsion speed that is proportional to the concentration of bound motors, and only when detached from the MT can the motors diffuse in the 2D

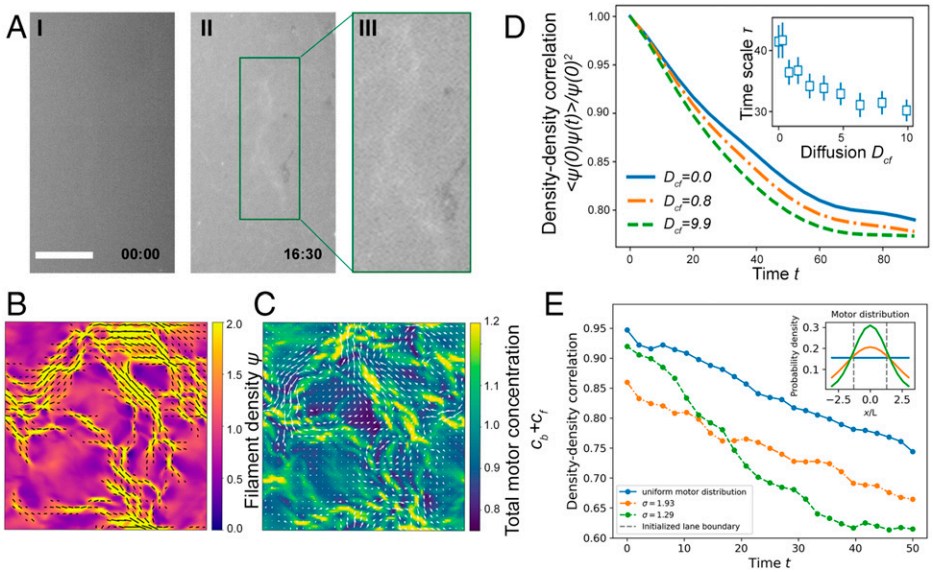

Fig. 5. Effect of diffusion on kinesin and MT distribution. Local kinesin concentration is enriched due to MT gliding. (*A*) An experimental example of kinesin redistribution in the lipid bilayer substrate in response to a MT-enriched lane. At time t = 0 s (I) GFP-labeled kinesin in the membrane is very uniform in distribution. After 16 min and 30 s significant inhomogeneities emerge in kinesin distribution in the same area (II, III). The kinesin distribution is not correlated with individual MTs. (Scale bar, 20 μm.) (*B* and *C*) Snapshots of lane formation from hydrodynamic simulations with motor kinetics. (*B*) Filament density is shown as the color code and black lines show the direction of the nematic director field. (*C*) Color code shows the total motor concentration and white arrows show the direction of the polarization field which mostly point toward the lanes indicating that there is a preferential inflow of filaments into the motor and filament density rich regions (see Movie S6). (*D*) Density–density correlation as function of time for different values of motor diffusion constant measured in the hydrodynamic simulations. (*Inset*) Decorrelation time scale (in simulation units given by the diffusion time scale α_p^{-1}) extracted from the density-density correlation function for varying motor diffusion. (*E*) Density–density correlation as a function of time, obtained from Brownian dynamics simulations of 100 filaments (length L) initialized as a single bidirectional lane along the *y* direction (lane width = 2.58) for different static Gaussian (width σ) or uniform motor distributions plotted in the inset. Time is plotted in units of L/v_0.

plane. Such a dependence of propulsion velocity agrees to first order with the experimentally measured velocity dependence of MTs driven by kinesin motors (in the linear regime far from saturation) (17).

Our model captures the observed phenomenon of motors colocalizing with filament lanes shown in Fig. 5*A*. The results of the corresponding simulations are shown in Fig. 5*B* in which filament density is color-coded with the nematic director as black lines. Fig. 5*C* shows total motor concentration with the polarization field as white arrows, and the images reveal clear colocalization of filament density with motor density.

Furthermore, we investigated how the diffusion constant of free kinesin motors D_{cf} affects the dynamical behavior of simulated lanes by calculating the density–density correlation function $<\psi(0)\ \psi(t)>$. Here $<.>$ denotes a space average and ψ is the density of filaments. Fig. 5*D* shows the density–density correlation function for different values of D_{cf} . At finite motor diffusion, $<\psi(0)\ \psi(t)>$ decorrelates faster than for zero diffusion, which shows that the density and therefore the lanes become more dynamic in the presence of motor diffusion. To further quantify the decorrelation of nematic lanes we extracted decorrelation time scales τ from the density–density correlation functions. Fig. 5*D*, *Inset* shows the decorrelation time scale for different kinesin motor diffusion constants. We find that the addition of motor diffusion reduces this density decorrelation time scale and hence increases movement of the lanes. This result is consistent with the experiments, where we qualitatively observed that the lanes are not spatially fixed and can move or dissolve and reform over time (Movies S1 and S2). Our modeling predicts a speedup in lane turnover dynamics as membrane fluidity increases (Fig. 5*D*), which can be contrasted with the relatively stable lanes seen on glass in ref. 24 (static over ∼100 s). This is an additional feature of gliding assays on fluid membranes apart from suppressed filament cross-overs.

The connection between enhanced lane dynamics and motor mobility is related to the fact that motors and filaments are colocalized as demonstrated in Fig. 5 *A*–*C* and Movie S6. Motors that diffuse while unbound spend more time in regions where they are more often bound to filaments because filament density is locally higher, such as in lanes. However, a locally higher concentration of motors creates an inhomogeneous activity field for the filaments, increasing the flux of filaments out of the lane toward regions of lower motor concentration, and thus speeding up the shifting and disappearance of each lane. To further investigate the latter point, we conducted microscopic, agent-based Brownian dynamics simulations of active, semiflexible, mutually repulsive filaments representing MTs, which were initialized in a bidirectional lane. The filaments experience an active self-propulsion force only near discrete point-particle motors, which are held in a static but nonuniform distribution (see *SI Appendix*). This approach (Fig. 5*E*) revealed that filament density–density correlations $<\psi(t)\ \psi(0)>$ diminish more rapidly when the motor distribution has steeper gradients, indicating faster loss of the initial lane, even though the total number of motors was kept fixed. This supports our interpretation of the mesoscale hydrodynamic simulation results with regard to the experiment: Inhomogeneous motor concentrations due to motor diffusion are expected to speed up the dynamics of MT lanes, relative to the case of fixed motors in a uniform distribution. In effect, while motors are recruited to MT lanes, the MTs tend to deplete from local increases in motor density, enhancing the rate at which lanes shift, dissolve, and reform.

Conclusion

In this paper we demonstrate the formation of two different active MT states: dynamic apolar lanes and an active nematic. These states occur spontaneously in a crowded layer of gliding

MTs attached to a fluid membrane substrate. Our analysis of MT interaction statistics demonstrates a "weak," angle-dependent alignment effect induced by active collisions and compares well with recently published work using F-actin filaments (30) in which subtle tuning of parameters can elicit a global organizational change. These nematic phases are distinct from the widely studied active nematics dominated by topological defects introduced by Sanchez et al. (20).

We use an experimental geometry in which kinesin motors are directly coupled to lipids in a fluid bilayer substrate and show that the fluid membrane substrate allows for lateral motor diffusion, which can impact the motion of the gliding MTs. In an interesting feedback mechanism, gliding MTs also restructure the distribution of kinesin motors in the membrane. The lipid bilayer has an additional role in promoting the onset of active phase formation, inducing filament–filament alignment in the gliding layer via active bundling, without the use of added molecular depletants.

Biologically, this work may have implications in analogous contexts where motile or dynamic filaments are coupled to a surface—for example, in the way that the motor-induced activity of cytoskeletal filaments helps to organize structures on the cell membrane through cytoskeleton–membrane interactions (43, 44), in cortical MT arrays in plant cells, or for MreB (an actin homolog) arrays in bacteria (45, 46).

Combining experimental observations with hydrodynamic theory and numerical simulations we tuned the MT, kinesin, and ATP (activity) concentrations to show that increasing motor activity promotes lane formation and speeds up lane dynamics; while consistent with previous work (24), increasing MT density of the membrane surface plays a crucial role in lane formation and the onset of the active nematic phase. Most strikingly, we observed that with motors able to diffuse through the substrate the motor density is enriched at the lanes, yet this inhomogeneity serves to destabilize those very lanes, representing an interesting interplay between positive and negative mechanochemical feedback. Our system thus presents an excellent platform for a new perspective on the study of active matter with spatiotemporal activity variations (13, 47–49). The effective activity of the aligning biopolymers depends on an energy-consuming second population of macromolecules (the motors) whose distribution is continually reorganized by the very active matter dynamics that it enables. The system can therefore be tuned between a pattern-forming gliding assay and an assay exhibiting a spatially homogeneous active nematic as a function of MT density, thereby introducing a paradigm that bridges the gap between these two types of experiments. This kind of self-organized behavior can point to new ways to engineer dynamic and reconfigurable materials where the structural elements and power sources can dynamically colocalize, maximizing efficiency and enabling self-repairing structures capable of efficient mechanical work.

Materials and Methods

Supported Lipid Bilayer Preparation. Glass slides and coverslips were cleaned by sonication for 1 h each in acetone, methanol, and ethanol then rinsed thoroughly with deionized water. Glass slides and coverslips were also plasma-cleaned (Harrick Plasma PDC-002) for 7 min immediately prior to experiments. The lipid mixture was composed of 90 mol % DOPC, 10 mol % DGS-NTA(Ni) in chloroform or 89.95 mol % DOPC, 10 mol % DGS-NTA(Ni), and 0.05 mol % Cy5 PC (fluorescent lipid) in chloroform. The lipid mixture was placed under vacuum for 4 h to remove all chloroform. Lipids were rehydrated with nanopure water to a final concentration of 2.5 mM. To make a supported lipid bilayer, the vesicle fusion method was used. In order to make small unilamellar vesicles (SUVs) the hydrated lipid was sonicated for 5 min under the tip sonicator. SUVs were drop-cast on a clean flow chamber and stayed placed in an oven at 50° C for 1 h to let vesicles form a lipid bilayer on the glass with a hydration layer beneath. The flow chamber was constructed using a spacer (Grace Bio-Labs) stuck to the clean glass slide (75 × 25 mm) with a cut in the middle to make a water layer and a coverslip (22 × 22 mm) on top of the spacer. Buffer exchange was allowed from two sides of the coverslip. Lipid bilayers were confirmed using fluorescent microscopy and FRAP. All lipids used in this work were purchased from Avanti Polar Lipids in chloroform and used without further purification, including 1,2-dioleoyl-*sn*-glycero-3-phosphocholine (DOPC), 1,2- dioleoyl-*sn*-glycero-3-[(*N*-(5-amino-1-carboxypentyl) iminodiacetic acid) succinyl] (nickel salt) DGS-NTA(Ni), and 1,2-dioleoyl-*sn*-glycero-3-phosphocholine-*N*- (Cyanine 5). In order to anchor motor proteins to the lipid bilayer, a lipid with 10 mol % DGS-NTA(Ni) (lipid 1,2-dioleoyl-*sn*-glycero-3-[(*N*-(5-amino-1-carboxypentyl) iminodiacetic acid) succinyl] (nickel salt) was included.

Protein Preparation. Unlabeled porcine tubulin purified with high concentration Pipes buffer was prepared using a previously reported protocol (8). Rhodamine labeled tubulin was purchased from Cytoskeleton Inc. and suspended in 5 mg/mL in PEM80 buffer (80 mM Pipes, 1 mM ethylene glycol bis (-aminoethyl ether), 1 mM $MgSO_4$, pH 6.9), and polymerized with 10 mM GTP, stabilized with 1 mM taxol. To polymerize the tubulin to an average MT length of 7.3 ± 0.73 μm, the solution was incubated in a 37 °C water bath for 1 h and MTs were kept in a dark box at room temperature. Recombinant penta-histidine-tagged kinesin proteins were purified from *Escherichia coli* as previously reported (11, 18).

MT Gliding. Green fluorescent protein (GFP)-tagged kinesin at a concentration of 300 nM was introduced to the flow cell and incubated for 10 min to allow motor proteins to bind to the lipid bilayer. Next, we prepared different solutions of labeled and unlabeled MTs. The solution is introduced to the flow cell and incubated for another 10 min. Finally, we added motility mix to wash away the excess and unbounded proteins, provide energy for the system, and reduce photobleaching. Motility mix includes PEM80 buffer with 1 mM ATP, 1 mM dithiothreitol, 10 μM taxol, 0.22 mg/mL glucose oxidase, 0.04 mg/mL catalase, 3.68 mg/mL glucose, 2 mM phosphocreatine, and 70 g/mL creatine phosphokinase. The flow cell is sealed with ultraviolet glue before imaging to prevent leakage. We can estimate the surface density of motors on the bilayer to be 25.4 ± 0.62 μm^{-2} as calculated in a recent publication by our group using an identical experimental setup (16).

Image Acquisition and Analysis. For experimental imaging we used fluorescence microscopy (DM 2500P fluorescence microscope; Leica Microsystems Inc.) and confocal fluorescence microscopy (Zeiss LSM 889 with AiryScan + FAST and a Gallium arsenide phosphide [GaAsP] photon-counting photodetector). A QImaging Retigia Exi camera and an ORCA - Flash4.0 LT+ Digital CMOS camera, (Hamamatsu) were used to record fluorescence movies under low-light conditions. The images were recorded at 10-s time intervals with either 20×, 40×, or 63× objectives. For the phase diagram in Fig. 3*A* we used a region of interest (ROI) of 500 pixels × 500 pixels (where 2.1 pixels = 1 μm) and the following order parameter thresholds to determine the phase behavior: Nematic $S > 0.25$, Coexistence $0.20 < S < 0.25$, Lane formation $0.10 < S < 0.20$, and Isotropic $0 < S < 0.10$. In Fig. 3 *C* and *D* we calculated the nematic order parameter and the ROI box size was varied to compare local and global order parameters. Image analysis was performed using ImageJ (https://imagej.nih.gov/ij/) including the ImageJ plugin OrientationJ to calculate angular distributions of MTs (23). Order parameters in each image were calculated using the formula below with the ImageJ plugin, OrientationJ and a bin size of 5° to calculate angular distributions of the MTs using the published method from Inoue et al. (23):

$$S = \frac{1}{N}\sqrt{\left(\sum_{i=1}^{36} R_i \cos 2\theta_i\right)^2 + \left(\sum_{i=1}^{36} R_i \sin 2\theta_i\right)^2}.$$

Here, N is the total number of distinct orientational angles calculated by the software for each frame. R is the frequency of the discretized angles, θ, and S is the calculated order parameter.

To calculate MT surface density on the bilayer, five different regions of area, A, are randomly selected for each flow cell. The MTs were counted manually for those selected regions and the fraction of fluorescently labeled MTs for each flow cell used to find the total MTs per unit area.

FRAP. To measure the bilayer-coupled diffusion constant, D_{KIN}, of the motor proteins, we used motors tagged with GFP (Addgene). The membrane lipids were not labeled. Measurements were carried out on a confocal laser scanning microscope (Zeiss LSM 880) using the ZEISS ZEN imaging software (ZEN Black, https://www.zeiss.com/microscopy/us/products/microscope-software/zen.html) to selectively bleach motors in a circular area of the membrane with diameter of 32.6 μm. The bleaching process is irreversible, but due to the effects of diffusion bleached motors are gradually replaced by unbleached motors, resulting

in a recovery of fluorescence intensity in the bleached area over time. To obtain a diffusion constant for the motors, we measured the normalized intensity of the bleached region as a function of time, fitting the Soumpasis diffusion equation (50–52):

$$D = \frac{\omega^2}{\tau_{1/2}},$$

where the diameter of the bleached area (ω) was 32.6 μm and the intensity half-life ($\tau_{1/2}$) was 155.7 s.

Collision Statistics Analysis. To obtain collision statistics, we used microscopic image sequences of length 85 frames (with time interval of 10 s between frames), each of size 662.86 $\times$ 495.24 μm. To clearly observe individual MTs and collisions, we further zoomed into these images and used a field of view of 165 $\times$ 123 μm. To minimize any bias in sampling we scanned our field of view across the entire image and collected collision samples from different regions. We measured angles between colliding MTs taking their direction of movement into account as done in a previous study (23). The angle between filaments was measured right before their collision (when the filaments are seen to be separate) and right after collision (if they crossed over) or after they were observed to move parallel or antiparallel for at least 20 s (if they were bundled together). In the case of active bundling the output angle was taken to be 0 (if they were observed to move parallel) or 180° (if they are antiparallel). We collected input and output angles for 100 collision events each for lipid and glass. We then computed the fraction of these events that correspond to active bundling (output angle 0 or 180) or crossing over (output angle not 0 or 180).

Continuum Model for Active Filament and Motor Kinetics. The dynamics of the three key hydrodynamic variables obtained by coarse-graining the equations of motion of a collection of self-propelled rods, supplemented by a phenomenological description of the density-driven nematic transition, are specified by

$$\partial_t \psi = -\partial_i(v p_i) + D_\psi \nabla^2 \psi \; + \; \Gamma_\psi \nabla^2 \frac{\delta F}{\delta \psi}$$

$$\partial_t p_i = -\partial_j \left(v \left(Q_{ij} + \frac{1}{2}\delta_{ij}\psi \right) \right) - \alpha_p p_i$$

$$\partial_t Q_{ij} = \left(\delta_{ij}\partial_k v p_k - \partial_i v p_j - \partial_j v p_i \right) - \Gamma_p \frac{\delta F}{\delta Q_{ij}},$$

where v is the spatially local propulsion speed set by the density of motors bound to the filaments, c_b, as $v = v_0 c_b / c_{bo}$, with v_0 is the characteristic speed set by a characteristic bound motor density, c_{bo}. D_ψ and α_p correspond to the translational and rotational diffusion of filaments. F represents the usual Landau–de Gennes free energy describing nematic elasticity and the isotropic-nematic transition but is coupled to filament density, so that the nematic phase occurs at sufficiently high values of ψ:

$$F = \frac{\beta_Q}{4} Q_{ij}^2 \left(\frac{Q_{kh}^2}{4} + 1 \right) - \frac{C_Q}{4} Q_{ij}^2 \psi + \frac{\kappa}{2} \left(\partial_k Q_{ij} \right)^2.$$

The values of the parameters in the model, including total filament density, are chosen so that the equilibrium phase has bulk nematic order above a critical concentration, $\psi_c = \beta_Q / C_Q$, which is chosen as the unit of density in the simulations. See *SI Appendix* for a table listing and justification of the parameter values used in the simulation. Long-range hydrodynamic flows are assumed damped by substrate friction from the membrane. The motors are allowed to bind to and unbind from the filaments, and only the free motors can diffuse on the lipid membrane. The kinetics for the density of bound (c_b) and free (c_f) motors is then given by

$$\partial_t c_f = D_{c_f} \nabla^2 c_f - k_{on} c_f \psi + k_{off} c_b$$

$$\partial_t c_b = k_{on} c_f \psi - k_{off} c_b.$$

The dynamic equations are numerically integrated from random initial conditions using a finite differences method with fourth-order Runge–Kutta time updates and employing periodic boundary conditions.

Brownian Dynamics Simulation. Brownian dynamics was used to simulate MTs, represented as active bead-spring chains (29, 53) gliding in the presence of a static, spatially nonuniform distribution of kinesin motors represented as point particles. The motor distributions were generated probabilistically using Gaussian or uniform spatial distributions. For the MTs, Hookean spring restoring forces were used both for the bonds connecting adjacent beads and for the angles between consecutive bonds, the latter giving the chain a bending rigidity. An active force pushes a bead in the filament's local tangent direction if there is a motor within a threshold distance from the center of the bead. The Weeks–Chandler–Andersen potential was used for steric repulsions between beads of different chains. Positions were updated using a second-order stochastic Runge–Kutta time update (54). A detailed description of the model, including a list of parameters and equations of motion, is given in *SI Appendix*.

Data Availability. The data that support the findings of this study are openly available in Dryad at https://doi.org/10.6071/M37088. Code for implementing continuum model and agent based simulations are available upon reasonable request to the authors.

ACKNOWLEDGMENTS. We thank David Quint for help with image analysis. The data in this work were collected, in part, with a confocal microscope acquired through NSF MRI Award DMR-1625733. We acknowledge generous funding from the NSF. L.S.H. acknowledges DMR-1808926 and A.G. acknowledges support from DMS-1616926 and CMMI-1548571. The project was also supported by NSF-CREST: Center for Cellular and Biomolecular Machines at the University of California, Merced (HRD-1547848) and by the Brandeis Biomaterials Facility (DMR-2011486). M.G.A. and D.A.B. were supported by the Hellman Fellows Fund. We gratefully acknowledge computing time on the Multi-Environment Computer for Exploration and Discovery (MERCED) cluster (NSF Grant No. ACI-1429783).

1. R. Phillips, J. Kondev, J. Theriot, H. Garcia, *Physical Biology of the Cell* (Taylor & Francis Group, New York, 2008).
2. D. Needleman, Z. Dogic, Active matter at the interface between materials science and cell biology. *Nat. Rev. Mater.* **2**, 17048 (2017).
3. D. Nishiguchi, K. H. Nagai, H. Chaté, M. Sano, Long-range nematic order and anomalous fluctuations in suspensions of swimming filamentous bacteria. *Phys. Rev. E* **95**, 020601 (2017).
4. R. Aditi Simha, S. Ramaswamy, Hydrodynamic fluctuations and instabilities in ordered suspensions of self-propelled particles. *Phys. Rev. Lett.* **89**, 058101 (2002).
5. T. B. Liverpool, M. C. Marchetti, Rheology of active filament solutions. *Phys. Rev. Lett.* **97**, 268101 (2006).
6. J. F. Joanny, F. Jülicher, K. Kruse, J. Prost, Hydrodynamic theory for multi-component active polar gels. *New J. Phys.* **9**, 422 (2007).
7. M. Soares e Silva *et al.*, Active multistage coarsening of actin networks driven by myosin motors. *Proc. Natl. Acad. Sci. U.S.A.* **108**, 9408–9413 (2011).
8. L. Farhadi *et al.*, Active self-organization of actin-microtubule composite self-propelled rods. *Front. Phys.* **6**, 1247 (2018).
9. V. Schaller, C. Weber, C. Semmrich, E. Frey, A. R. Bausch, Polar patterns of driven filaments. *Nature* **467**, 73–77 (2010).
10. M. Fritzsche *et al.*, Self-organizing actin patterns shape membrane architecture but not cell mechanics. *Nat. Commun.* **8**, 14347 (2017).
11. A. J. Tan, D. E. Chapman, L. S. Hirst, J. Xu, Understanding the role of transport velocity in biomotor-powered microtubule spool assembly. *RSC Adv.* **6**, 79143–79146 (2016).
12. M. Fritzsche *et al.*, Cytoskeletal actin dynamics shape a ramifying actin network underpinning immunological synapse formation. *Sci. Adv.* **3**, e1603032 (2017).
13. T. D. Ross *et al.*, Controlling organization and forces in active matter through optically defined boundaries. *Nature* **572**, 224–229 (2019).
14. Y. Sumino *et al.*, Large-scale vortex lattice emerging from collectively moving microtubules. *Nature* **483**, 448–452 (2012).
15. M. J. Schnitzer, S. M. Block, Kinesin hydrolyses one ATP per 8-nm step. *Nature* **388**, 386–390 (1997).
16. C. T. Friel, J. Howard, Coupling of kinesin ATP turnover to translocation and microtubule regulation: One engine, many machines. *J. Muscle Res. Cell Motil.* **33**, 377–383 (2012).
17. R. Grover *et al.*, Transport efficiency of membrane-anchored kinesin-1 motors depends on motor density and diffusivity. *Proc. Natl. Acad. Sci. U.S.A.* **113**, E7185–E7193 (2016).
18. J. Lopes *et al.*, Membrane mediated motor kinetics in microtubule gliding assays. *Sci. Rep.* **9**, 9584 (2019).
19. D. B. Stein, G. De Canio, E. Lauga, M. J. Shelley, R. E. Goldstein, Swirling instability of the microtubule cytoskeleton. *Phys. Rev. Lett.* **126**, 028103 (2021).
20. T. Sanchez, D. T. Chen, S. J. DeCamp, M. Heymann, Z. Dogic, Spontaneous motion in hierarchically assembled active matter. *Nature* **491**, 431–434 (2012).
21. A. J. Tan *et al.*, Topological chaos in active nematics. *Nat. Phys.* **15**, 1033–1039 (2019).
22. G. Duclos *et al.*, Topological structure and dynamics of three-dimensional active nematics. *Science* **367**, 1120–1124 (2020).
23. D. Inoue *et al.*, Depletion force induced collective motion of microtubules driven by kinesin. *Nanoscale* **7**, 18054–18061 (2015).
24. L. Huber, R. Suzuki, T. Krüger, E. Frey, A. R. Bausch, Emergence of coexisting ordered states in active matter systems. *Science* **361**, 255–258 (2018).
25. S. Tanida *et al.*, Gliding filament system giving both global orientational order and clusters in collective motion. *Phys. Rev. E* **101**, 032607 (2020)
26. M. Abkenar, K. Marx, T. Auth, G. Gompper, Collective behavior of penetrable self-propelled rods in two dimensions. *Phys. Rev. E Stat. Nonlin. Soft Matter Phys.* **88**, 062314 (2013).
27. H. Chaté, Dry aligning dilute active matter. *Annu. Rev. Condens. Matter Phys.* **11**, 189–212 (2020).
28. J. Denk, E. Frey, Pattern-induced local symmetry breaking in active-matter systems. *Proc. Natl. Acad. Sci. U.S.A.* **117**, 31623–31630 (2020).

PHYSICS

29. J. M. Moore, T. N. Thompson, M. A. Glaser, M. D. Betterton, Collective motion of driven semiflexible filaments tuned by soft repulsion and stiffness. *Soft Matter* **16**, 9436–9442 (2020).
30. A. Sciortino, A. R. Bausch, Pattern formation and polarity sorting of driven actin filaments on lipid membranes. *Proc. Natl. Acad. Sci. U.S.A.* **118**, e2017047118 (2021).
31. X. Shi, H. Chaté, Self-propelled rods: Linking alignment-dominated and repulsion-dominated active matter. arXiv [Preprint] (2018). https://arxiv.org/abs/1807.00294 (Accessed 13 December 2021).
32. A. von Massow, E. M. Mandelkow, E. Mandelkow, Interaction between kinesin, microtubules, and microtubule-associated protein 2. *Cell Motil. Cytoskeleton* **14**, 562–571 (1989).
33. L. Onsager, The effects of shape on the interaction of colloidal particles. *Ann. N. Y. Acad. Sci.* **51**, 627–659 (1949)
34. F. Ginelli, F. Peruani, M. Bär, H. Chaté, Large-scale collective properties of self-propelled rods. *Phys. Rev. Lett.* **104**, 184502 (2010).
35. A. Baskaran, M. C. Marchetti, Hydrodynamics of self-propelled hard rods. *Phys. Rev. E Stat. Nonlin. Soft Matter Phys.* **77**, 011920 (2008).
36. M. Bär, R. Großmann, S. Heidernreich, F. Peruani, Self-propelled rods: Insights and perspectives for active matter. *Annu. Rev. Condens. Matter Phys.* **11**, 441–466 (2020).
37. H. H. Wensink, H. Löwen, Emergent states in dense systems of active rods: From swarming to turbulence. *J. Phys. Condens. Matter* **24**, 464130 (2012).
38. R. Großmann, I. S. Aranson, F. Peruani, A particle-field approach bridges phase separation and collective motion in active matter. *Nat. Commun.* **11**, 5365 (2020).
39. I. Maryshev, A. B. Goryachev, D. Marenduzzo, A. Morozov, Dry active turbulence in a model for microtubule-motor mixtures. *Soft Matter* **15**, 6038–6043 (2019).
40. A. Peshkov, I. S. Aranson, E. Bertin, H. Chaté, F. Ginelli, Nonlinear field equations for aligning self-propelled rods. *Phys. Rev. Lett.* **109**, 268701 (2012).
41. E. Bertin *et al.*, Mesoscopic theory for fluctuating active nematic. *New J. Phys.* **15**, 085032 (2013).
42. S. Tsitkov, Y. Song, J. B. Rodriguez III, Y. Zhang, H. Hess, Kinesin-recruiting microtubules exhibit collective gliding motion while forming motor trails. *ACS Nano* **14**, 16547–16557 (2020).
43. D. V. Köster *et al.*, Actomyosin dynamics drive local membrane component organization in an in vitro active composite layer. *Proc. Natl. Acad. Sci. U.S.A.* **113**, E1645–E1654 (2016).
44. D. Gaswami *et al.*, Nanoclusters of GPI-anchored proteins are formed by cortical actin-driven activity. *Cell* **135**, 1085–1097 (2008).
45. R. Dixit, R. Cyr, The cortical microtubule array: From dynamics to organization. *Plant Cell* **16**, 2546–2552 (2004).
46. S. van Teeffelen *et al.*, The bacterial actin MreB rotates, and rotation depends on cell-wall assembly. *Proc. Natl. Acad. Sci. U.S.A.* **108**, 15822–15827 (2011).
47. S. Shankar, C. M. Merchetti, Hydrodynamics of active defects: From order to chaos to defect. *Phys. Rev. X* **9**, 041047 (2019).
48. R. Zhang *et al.*, Structuring stress for active materials control. arXiv [Preprint] (2019). https://arxiv.org/abs/1912.01630 (Accessed 13 December 2021).
49. F. J. Schwarzendahl, P. Ronceray, K. L. Weirich, K. Dasbiswas, Self-organization and shape change by active polarization in nematic droplets. *Phys. Rev. Res.* **3**, 043061 (2021).
50. D. Axelrod, D. E. Koppel, J. Schlessinger, E. Elson, W. W. Webb, Mobility measurement by analysis of fluorescence photobleaching recovery kinetics. *Biophys. J.* **16**, 1055–1069 (1976).
51. D. M. Soumpasis, Theoretical analysis of fluorescence photobleaching recovery experiments. *Biophys. J.* **41**, 95–97 (1983).
52. J. D. Lopes, "Membrane-bound kinesin transport and its applications in active matter," PhD thesis, University of California, Merced, CA (2019).
53. K. R. Prathyusha, S. Henkes, R. Sknepnek, Dynamically generated patterns in dense suspensions of active filaments. *Phys. Rev. E* **97**, 022606 (2018).
54. A. C. Brańka, D. M. Heyes, Algorithms for Brownian dynamics computer simulations: Multivariable case. *Phys. Rev. E* **60**, 2381 (1999).